

Molecularly Thin Polyaramid Nanomechanical Resonators

Hagen Gress,¹ Cody L. Ritt,² Inal Shomakhov,¹ Kaan Altmisdorf,¹ Michelle Quien,³ Zitang Wei,³ John R. Lawall,⁴ Narasimha Boddeti,⁵ Michael S. Strano,^{3,*} J. Scott Bunch,^{1,*} and Kamil L. Ekinci^{1,*}

¹*Department of Mechanical Engineering,
Division of Materials Science and Engineering, and the Photonics Center,
Boston University, Boston, Massachusetts 02215, USA*

²*Department of Chemical and Biological Engineering, University of Colorado Boulder, Boulder, Colorado 80309, USA*

³*Department of Chemical Engineering, Massachusetts Institute of Technology,
Cambridge, Massachusetts 02139, USA*

⁴*National Institute of Standards and Technology, Gaithersburg, Maryland 20899, USA*

⁵*Washington State University, School of Mechanical and Materials Engineering,
Pullman, Washington 99163, USA*

(Dated: January 21, 2026)

Abstract: Two-dimensional polyaramids exhibit strong hydrogen bonding to create molecularly thin nanosheets analogous to graphene. Here, we report the first nanomechanical resonators made out of a two-dimensional polyaramid, 2DPA-1, with thicknesses as small as 8 nm. To fabricate these molecular-scale resonators, we transferred nanofilms of 2DPA-1 onto chips with previously-etched arrays of circular microwells. We then characterized the thermal resonances of these resonators under different conditions. When there is no residual gas inside the 2DPA-1-covered microwells, the eigenfrequencies are well-described by a tensioned plate theory, providing the Young's modulus and tension of the 2DPA-1 nanofilms. With gas present, the nanofilms bulge up and mechanical resonances are modified due to the adhesion, bulging and slack present in the system. The fabrication and mechanical characterization of these first 2DPA-1 nanomechanical resonators represent a convincing path toward molecular-scale polymeric NEMS with high mechanical strength, low density, and synthetic processability.

Keywords: NEMS, 2D material, polymer, nanomechanical resonator, Brownian motion, adhesion energy

Nanoelectromechanical Systems (NEMS) or nanomechanical resonators are evolving both in functionality and form since the first NEMS devices etched out of silicon in the 1990s [1, 2]. An overarching research theme in the field has been the exploration of different materials for NEMS. New materials with extraordinary properties have allowed for superior resonator parameters as well as the reduction of resonator linear dimensions. NEMS made out of one- and two-dimensional (2D) nanomaterials — with unique mechanical, electronic, chemical, and optical properties — have opened the door for devices with linear dimensions well below the limits of lithography and functionalities well beyond those of semiconductors and metals [3–5]. So far, 2D NEMS have been fabricated from a variety of 2D crystalline nanomaterials, such as graphene [6], hexagonal boron nitride [7], transition metal dichalcogenides [8, 9], MXenes [10, 11], and nanoparticles [12–14]. Various polymeric materials have also been explored as mechanical resonators [15–20] — although these structures have typically remained far from molecular scale thicknesses. Converging these two approaches, i.e., creating molecular scale polymeric NEMS analogous to 2D crystalline NEMS, would open up a powerful new direction in the NEMS field.

Recently, a 2D polyaramid, called 2DPA-1 [21], was

synthesized. Molecular-scale disks of 2DPA-1 form by polycondensation of melamine and trimesoyl chloride in solution and assemble into aligned layers upon spin coating (Figure 1a). Each molecular layer is approximately $\sim 3.7 \text{ \AA} (= 370 \text{ pm})$ thick and stacks via hydrogen bonding to form near-molecular-thickness films with an rms surface roughness of 500 pm [21, 22]. Despite lacking crystallinity, these films possess mechanical and gas barrier properties that are closer to 2D crystalline nanomaterials, such as graphene, than conventional polymers [22], and can be transferred onto substrates just like graphene. In short, 2DPA-1 combines material properties of conventional 1D polymers and 2D inorganic crystalline nanomaterials, such as graphene; it also opens up a new class of 2D nanomaterials that can be tailored to specific applications using the tools of organic chemistry [23, 24]. Such tunability — for example, in gas permeability or in the incorporation of functional groups — could enable a wide range of future technologies requiring high sensitivity and selectivity. This motivates an exploration of various nanoscale devices that can be fabricated from these new 2D polymeric materials. To this end, we report the fabrication and measurement of the first nanomechanical resonators made out of 2DPA-1. In addition to demonstrating nanomechanical resonances, we determine the Young's modulus from the measured resonances; we also develop a mechanical model for a membrane resonator partially adhered to walls and estimate the adhesion energy (between the polymer and the substrate) from resonance frequencies of membranes delaminating from the

* Email: strano@mit.edu

* Email: bunch@bu.edu

* Email: ekinci@bu.edu

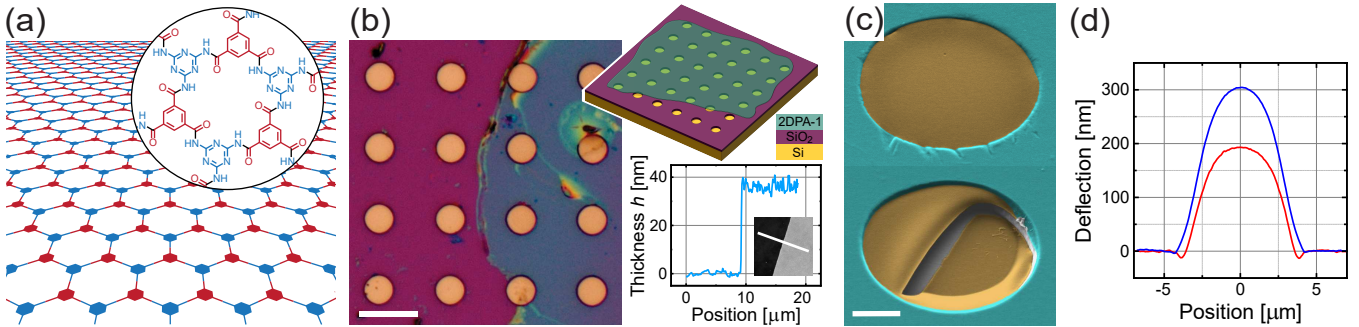


FIG. 1. (a) Illustration of an ideal 2DPA-1 monolayer with the molecular structure shown in the inset. (b) Optical microscope image of a typical sample showing the edge of the 2DPA-1 film. Microwells are etched into the SiO_2 layer on top of a Si substrate. A 2DPA-1 film is then transferred onto the chip through a wet process to create suspended membranes. The eight microwells on the left are not covered by the film. The scale bar is 20 μm . The top right inset shows an illustration of the sample. The bottom right inset shows an AFM line scan across the edge of a 35-nm-thick film, along the white line in the corresponding image. (c) SEM images of an intact (top) and a ruptured (bottom) 35-nm-thick membrane. The suspended region is false-colored in orange, and the rest is colored in blue. The scale bar is 2 μm . (d) AFM line scans through the center of 35-nm-thick circular membranes of radius 4.25 μm at atmospheric pressure. The data were taken within one hour after the membranes were removed from a high pressure chamber filled with nitrogen at 50 kPa (red) and 100 kPa (blue) above atmospheric pressure. Note the region adhered on the wall in the red curve.

substrate walls.

Figure 1b and 1c respectively show optical and scanning electron microscope (SEM) images of our nanomechanical drum resonators. Here, 2DPA-1 films are transferred onto SiO_2 substrates via wet transfer [21]. The substrates have arrays of etched microwells with depths of $g = 960$ nm and radii R of either 4.25 μm or 2.75 μm . In Figure 1b, the 2DPA-1 film partially covers the chip. The right insets show an illustration (top) and an AFM line scan (bottom) across the edge of the film. The SEM images in Figure 1c show an intact (top) and a broken (bottom) membrane with $R = 4.25$ μm and thickness $h = 35$ nm.

The samples in this study are measured in two distinct pressure states: i) nearly flat with very low gas pressure on either side, and ii) bulged with finite gas pressure p_{in} inside the microwell and very low pressure p_{ext} outside. Although the membranes are highly impermeable [22], gas transport into and out-of the microwell can take place through the interface between the polymer film and the substrate [25–27]. When the samples are placed in a high pressure gas chamber ($p_{ext} = 120 - 300$ kPa), the gas leaks into the microwell through the interface [22]. Once the sample is transferred to a low pressure environment (vacuum chamber or atmosphere), the pressure difference, $\Delta p = p_{in} - p_{ext}$, across the membrane causes it to initially bulge up. Figure 1d shows two AFM line scans of membranes at atmospheric pressure shortly after removal from a high pressure chamber. When brought to atmospheric pressure, bulged membranes gradually deflate on timescales ranging from minutes to several years [22]. If the samples are put in a low pressure chamber (i.e., $p_{ext} \approx 0$), the gas inside the microwell eventually leaks out, allowing the membrane to deflate to a nearly flat state. When $\Delta p = 0$, the membrane may be partially

adhered to the inside wall of the microwell (Figure 1c) in a stretched configuration with tension. If Δp is increased, the membrane starts to delaminate from the wall (Figure 1d), which typically introduces some slack [28–30]. We analyze both states in systematic experiments below.

We first measure the Brownian motion, i.e., thermal displacement fluctuations, of nearly flat membranes in vacuum. We achieve the flat state by placing the samples into a chamber maintained at a vacuum of $\sim 10^{-7}$ Torr (10^{-5} Pa) by an ion pump, which results in $p_{in} \approx p_{ext} \sim 10^{-7}$ Torr. The membranes display detectable thermal resonances for the first few eigenmodes (m, n) due to the relatively low dissipation with resonance frequencies f_{mn} and quality factors Q_{mn} . We use a path-stabilized homodyne Michelson interferometer to measure the thermal resonances at an antinode of each mode [31]. Details of the measurement process can be found in the Supporting Information file. Figure 2a shows the power spectral density (PSD) of the displacement fluctuations of the first four eigenmodes of a membrane with $R = 4.25$ μm and $h = 35$ nm. For $m \neq 0$, two nominally degenerate modes exist. If the resonator geometry deviates from an ideal circle, the resonance frequencies of these modes can split — as noticeable for the modes (1, 1) and (2, 1) in Figure 2a. The split modes can be clearly resolved by changing the angular position of the laser spot on the membrane. We fit each peak with a Lorentzian curve to determine f_{mn} and Q_{mn} .

To analyze the eigenfrequencies, we turn to the equation for the free transverse vibrations of a uniform circular plate under tension with radius R , thickness h , density ρ , tension S , and bending stiffness $D = \frac{Eh^3}{12(1-\nu^2)}$, where E is the Young's modulus and ν is the Poisson's ratio:

$$\rho h \frac{\partial^2 W}{\partial t^2} + \frac{D}{R^4} \nabla^4 W - \frac{S}{R^2} \nabla^2 W = 0. \quad (1)$$

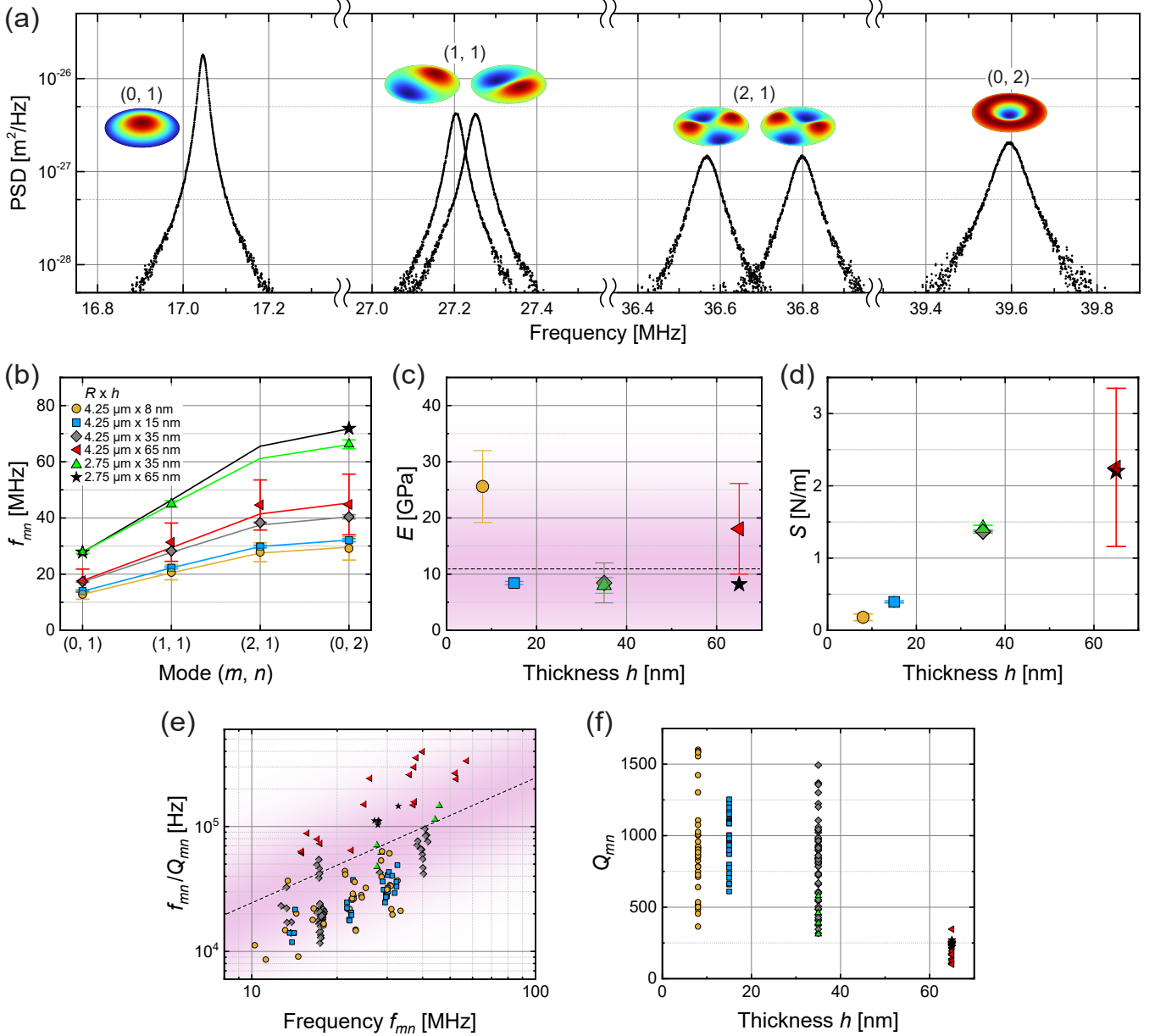


FIG. 2. (a) PSD of displacement fluctuations of the first four modes of a membrane with $R = 4.25 \mu\text{m}$ and $h = 35 \text{ nm}$. (b) Resonance frequencies f_{mn} for membranes with indicated R and h . The lines show the theoretical frequencies of the first four modes calculated using Eq. (2). (c) Young's modulus E and (d) tension S of the membranes shown in (b) as a function of thickness h . The dashed line and the shading respectively indicate the mean and spread of data with the Young's modulus being $E = 11.2 \pm 8.8 \text{ GPa}$. (e) Dissipation constants $\frac{f_{mn}}{Q_{mn}}$ as a function of frequency for all measured modes. The shading highlights that $\frac{f_{mn}}{Q_{mn}} \propto f_{mn}$, and the dashed line is a linear fit through the origin. (f) Quality factors Q_{mn} of all measured modes as a function of 2DPA-1 thickness.

Here, ∇^2 is the Laplacian operator in cylindrical coordinates; $\nabla^4 = (\nabla^2)^2$; and $W(r, \theta)$ is the displacement at (r, θ) . The coordinate r has been normalized with R such that $0 \leq r \leq 1$. A dimensionless tension parameter $U = \frac{SR^2}{D} = \frac{12(1-\nu^2)SR^2}{Eh^3}$ emerges from Eq. (1) with the plate and membrane limits for $U \rightarrow 0$ and $U \rightarrow \infty$, respectively. Under clamped boundary conditions, Eq. (2)

yields the resonance frequency of each eigenmode as [32]

$$f_{mn} = \frac{\alpha_{mn}}{2\pi R} \sqrt{\frac{1}{\rho h}} \sqrt{S + \frac{\alpha_{mn}^2 D}{R^2}}. \quad (2)$$

The coefficient α_{mn} corresponds to the n^{th} root of

$$\alpha \frac{J_{m+1}(\alpha)}{J_m(\alpha)} + \beta \frac{I_{m+1}(\beta)}{I_m(\beta)} = 0, \quad (3)$$

where J_m and I_m are the regular and modified Bessel functions of the first kind, respectively, and $\beta = \sqrt{\alpha^2 + SR^2/D}$. As U becomes large, e.g., due to a large S or small h , the bending term drops out of Eq. (1), yielding the membrane eigenfrequencies

$$f_{mn} = \frac{\alpha'_{mn}}{2\pi R} \sqrt{\frac{S}{\rho h}}, \quad (4)$$

where α'_{mn} is the n^{th} root of the Bessel function J_m [33].

Figure 2b shows the resonance frequencies of multiple modes of membranes with different R and h . Each data point is obtained by averaging measurements from $1 \leq N \leq 10$ membranes on the same chip with the same linear dimensions. Tables S1-3 in the Supporting Information file list all measured f_{mn} and Q_{mn} . For some membranes, not all modes could be resolved due to low Q values and, in the case of smaller membranes, small displacement amplitudes.

As long as the frequencies of two modes of the same membrane are measured, we can find E and S by performing error minimization in a parametric sweep [31, 34]. For each possible combination of E and S , we calculate α_{mn} from Eq. (3) and the theoretical eigenfrequencies $f_{mn}^{(t)}$ from Eq. (2) for the first four eigenmodes. We then minimize the error between the experimental and theoretical frequencies as described in the Supporting Information file to find the E and S values. Figure 2c and d respectively show the E and S found from error minimization. Returning to Figure 2b, the lines show the theoretical f_{mn} based on the mean E and S values for a given R and h ; the agreement is very good. The values for E , S , and U , as well as the number N of resonators measured for each combination of R and h are listed in Table I. The resonators with $h = 65$ nm have large error bars for E and S due to the small sample size. For the resonators with $h = 8$ nm, the rigidity term in Eq. (2) becomes small compared to the tension term, thus making the tension term dominant and the estimate for E error-prone. In summary, we find the average value $E = 11.2 \pm 8.8$ GPa, which is in good agreement with $E = 12.7 \pm 3.8$ GPa obtained from nanoindentation measurements [21]. We also extracted E and S using a different approach but arrived at similar values, as described in the Supporting Information file.

Figure 2e shows the dissipation constant, $\frac{f_{mn}}{Q_{mn}}$, for all the measured modes. Even though there is spread in the data from different modes and devices, the dissipation constant seems to increase linearly with frequency, indicating that Q_{mn} is frequency independent. It has been argued [35] that surface and bulk dissipation respectively result in Q factors that should scale as $Q \propto h$ and $Q \propto \text{constant}$. In an effort to observe one of these trends, we plot all Q_{mn} data as a function of h (Figure 2f). The thickest polymer devices appear to have the lowest Q factors, although further experiments are needed for a conclusive statement.

TABLE I. Radius R , thickness h , Young's modulus E , tension S , and non-dimensional tension parameter U of the resonators in Figure 2b-d. The data are from N different resonators on the same chip.

$R \times h$ [$\mu\text{m} \times \text{nm}$]	E [GPa]	S [N/m]	U [\cdot]	N
4.25×8	25.58 ± 6.40	0.18 ± 0.05	3×10^3	6
4.25×15	8.42 ± 0.28	0.39 ± 0.01	3×10^3	5
4.25×35	8.44 ± 3.55	1.37 ± 0.02	8×10^2	10
4.25×65	18.07 ± 8.06	2.26 ± 1.09	9×10^1	3
2.75×35	8.80 ± 1.40	1.41 ± 0.04	4×10^2	3
2.75×65	8.20	2.20	9×10^1	1

To gain more insight into the effect of wall adhesion and delamination on the resonance frequency, we perform a second set of experiments with bulged membranes. First, we describe our model for the resonance of a bulged and partially adhered membrane. The illustration in Figure 3a shows three snapshots of the membrane cross-section along with the relevant coordinates, including the experimental time coordinate. Our mechanical model does not distinguish between inflating and deflating membranes, and we prefer to describe the phenomenon beginning with the final state (backward in time). At its final flat state ($\Delta p = p_{in} - p_{out} = 0$), the membrane is re-adhered to the inner wall of the microwell at $z = 0$. The z_1 level is selected such that the tension in the membrane becomes zero if the membrane is flat at z_1 . As the membrane separates from the wall starting at $z = 0$ toward z_1 due to $\Delta p > 0$, it maintains some of the initial tension and acquires some additional tension due to the bulging, with δ_c being the bulge height at the center with respect to $z = 0$. When the membrane is at z_1 , the tension is entirely due to bulging. Further delamination causes a slack being introduced into the membrane, which results in an increased δ_c . The tension in the membrane in these regimes is derived from a spherical cap model in the Supporting Information file and can be summarized as

$$S^*(z^*) = \begin{cases} z_1^* & \text{for } z^* = 0, \\ (z_1^* - z^*) + \frac{2}{3}(\delta_c^* - z^*)^2 & \text{for } 0 < z^* \leq z_1^*, \\ (z_1^* - z^*) + \frac{2}{3}(1 - z^* + z_1^*)(\delta_c^* - z^*)^2 & \text{for } z^* > z_1^*. \end{cases} \quad (5)$$

Here, we present the results in dimensionless form, where $S^*(z^*) = \frac{S(z^*)}{Bh}$, with $B = \frac{E}{1-\nu}$ being the biaxial modulus; the dimensionless length scales are $\delta_c^* = \frac{\delta_c}{R}$, $z^* = \frac{z}{R}$, and $z_1^* = \frac{z_1}{R}$. Using $S(z)$ in Eqs. (3) and (2) along with E , ρ , ν , and linear dimensions provides the resonance frequency of the bulged-up and delaminated membrane. We reemphasize that the model does not depend on the direction of time.

In our re-adhesion experiments, the membranes are put into a high pressure chamber filled with nitrogen at $p_{ext} = 200$ kPa for several days before being placed

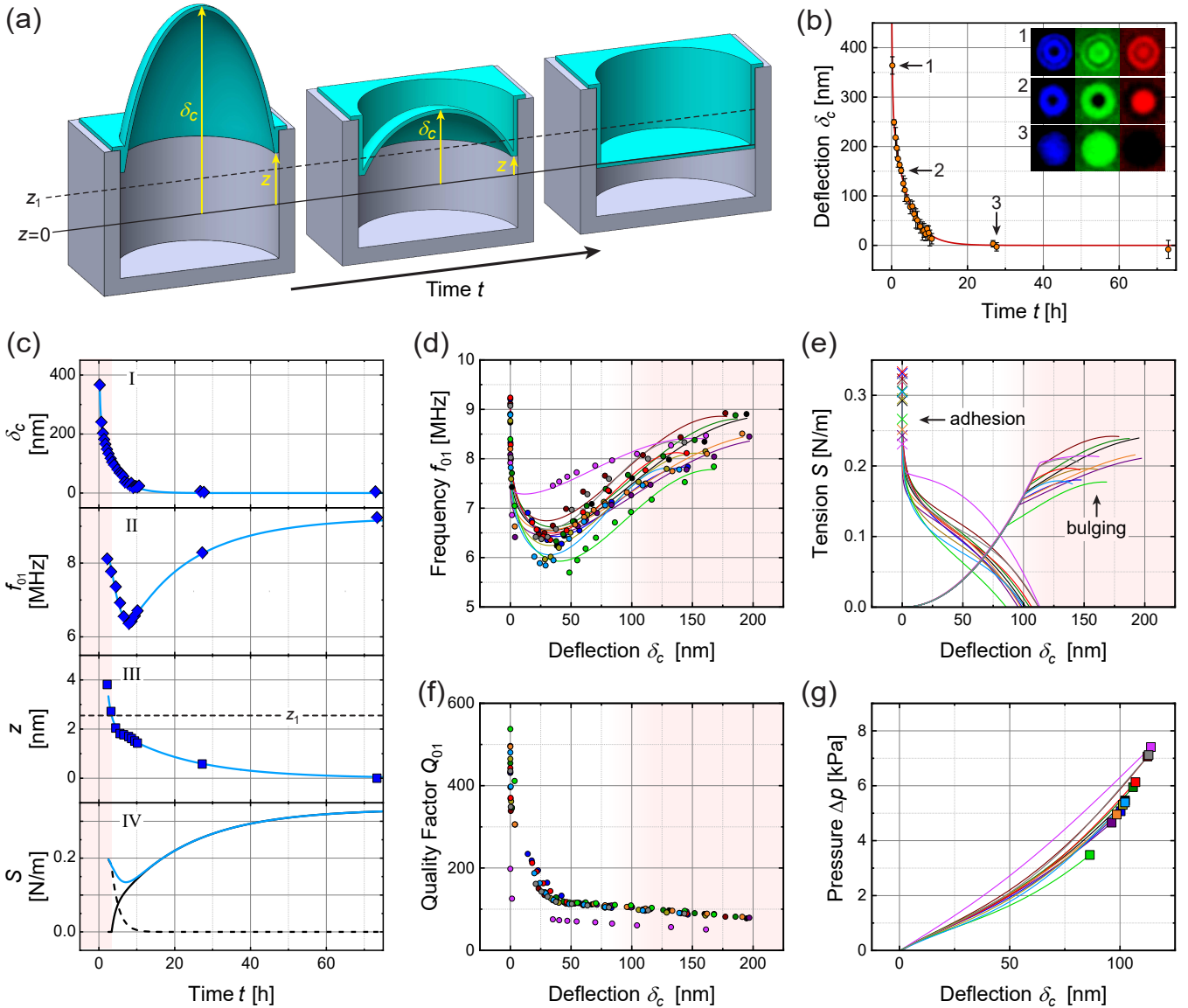


FIG. 3. (a) Illustration of a membrane at different stages of bulging. Note the time coordinate of our experiments. When $\Delta p = 0$ (right), the membrane is flat at $z = 0$ and stretched. For $\Delta p > 0$ (middle), the membrane is adhered to the wall to position $z > 0$ and bulges up by $\delta_c - z$. For $z > z_1$ (left), slack is introduced. Note that the illustration is not to scale; in the experiments, $z \ll \delta_c$. (b) Measured center deflection δ_c for a 35-nm-thick membrane with $R = 4.25 \mu\text{m}$ over time. The $\delta_c = 0$ line corresponds to the flat membrane at $z = 0$. The inset shows interferograms at wavelengths of 440 nm (blue), 540 nm (green), and 600 nm (red) for different δ_c as indicated by the arrows. (c) Time-dependent δ_c , f_{01} , z , and tension S for a 35-nm thick membrane. The shown values for z are calculated from measurements. The fit for z is an exponential function with two time constants, which is used to calculate the continuous curve in the frequency plot. The dashed line corresponds to the delamination length z_1 below which there is no slack. The total tension S (blue line) is comprised of a component due to bulging (black dashed line) and one due to wall adhesion (black solid line). The shading indicates the region of slack in the membrane. (d) Experimental data (symbols) and fits (lines) for f_{01} as a function of δ_c for twelve 35-nm-thick membranes, including the one in (c). The shaded regions indicate the range where slack exists in the membrane. (e) Tension components caused by bulging and wall adhesion as a function of δ_c , with the symbols representing the calculated tension at $z = 0$. (f) Quality factors Q_{01} as a function of δ_c . (g) Pressure Δp in the regime without slack ($z \leq z_1$) as a function of δ_c .

into the vacuum chamber ($p_{ext} \approx 0$). We measure the fundamental resonance frequency f_{01} and the quasistatic deflection field simultaneously as gas leaks out of the microwell slowly as a function of time. The deflection field is measured using full-field interferometry [36] with the

details given in the Supporting Information file. In the experiments, the membrane starts in a bulged-up and delaminated state (Figure 3a left). As the gas leaks out of the microwell, the membrane slowly deflates until the final flat state is reached (Figure 3a right). Figure 3b

shows the measured deflection δ_c at the center of a 35-nm-thick membrane over time, which can be fitted with an exponential decay function with two time constants. The asymptote corresponds to a flat membrane ($\delta_c = 0$, $z = 0$).

Figure 3c shows measured δ_c and f_{01} of a 35-nm-thick membrane as a function of time. Also shown are the calculated position z of the membrane on the wall, and the tension S . The analysis is performed as follows. At the last data point ($t \approx 75$ h), we assume $z = 0$ and determine $S(0)$ from the measured f_{01} using Eqs. (2) and (3) with $E = 12.7$ GPa and $\nu = 0.2$. Then, we find the value for z_1 as $\frac{Bh z_1}{R} = S(0)$. Once z_1 is found, we work our way through the rest of the frequency measurements with $\delta_c > 0$ and $z > 0$. We note that f_{01} depends on S through Eqs. (3) and (2); S , in turn, depends on z , δ_c and z_1 through Eq. (5). Thus, we can determine the z value for each f_{01} based on the measured δ_c and z_1 (Figure 3c III). The data points for z can be fitted with an exponential function with two time constants, which in turn allows us to generate continuous curves for other parameters. With z , δ_c and Eq. (5), we also determine the contributions of the tension terms (Figure 3c IV) due to bulging (dotted line) and due to wall adhesion (continuous black line).

Figure 3d shows the fundamental frequencies f_{01} of twelve 35-nm-thick membranes as a function of δ_c . The continuous curves are found from the model as described above, but plotted as a function δ_c instead of time. The respective contributions of the two tension terms are shown in Figure 3e. The sudden change in the slope of the bulging plots occurs at $z = z_1$ when slack is introduced to the system. Figure 3f shows the quality factors Q_{01} of the same twelve membranes. As the membranes deflate, Q_{01} increases due to decreased gas damping and increased tension due to adhesion.

Next, we estimate the pressure inside the microwell by focusing on the regime without slack ($0 \leq z \leq z_1$). In this regime, $\Delta p = p_{in} - p_{out} \approx p_{in}$ and can be determined as

$$\Delta p = Bh^*(\delta_c^* - z^*) \times \left[\frac{8}{3}(\delta_c^* - z^*)^2 + 4(z_1^* - z^*) + \frac{16}{3(1+\nu)}h^{*2} \right], \quad (6)$$

where $h^* = \frac{h}{R}$. The derivation for Eq. (6) can be found in the Supporting Information file. Figure 3g shows Δp as a function of δ_c .

Finally, the energy of adhesion of the membrane to the substrate can also be estimated, but only at the limit of a flat membrane, i.e., $z \approx 0$. At equilibrium, the total free energy change is

$$\frac{dW}{dz} + \frac{dF_s}{dz} + \frac{dF_a}{dz} = 0, \quad (7)$$

where all z derivatives are evaluated at $z = 0$. Here, $\frac{dW}{dz}$ is the incremental work done by the gas inside the microwell on the membrane; F_s is the strain energy stored

in the membrane; F_a is the free energy of adhesion. Figure 3g shows that $\frac{dW}{dz} = -\Delta p \frac{dV}{dz} \approx 0$, with V_b being the volume of the bulge, because $\Delta p \approx 0$ at $z = 0$. The strain energy is entirely due to the tension caused by wall adhesion [37],

$$F_s(z) \approx \pi B h (z_1 - z)^2, \quad (8)$$

and $\frac{dF_a}{dz} = 2\pi R \Gamma$ where Γ is the adhesion energy per unit area. Thus, in the limit of $z \approx 0$, this free energy model simply yields $\Gamma = B h \frac{z_1}{R} = S(0)$. We find the average value of $\Gamma = 0.29 \pm 0.04$ J/m².

The value for $S(0)$ and, therefore, Γ is lower for the deflating membranes (Figure 3e) compared to those that were never bulged by pressurization (Figure 2d). This observation can be explained by the history-dependence of the separation-adhesion process: hysteresis has been observed in separation-adhesion experiments on other 2D materials, where the energy of separation is significantly larger than the energy of adhesion [38]. In our experiments on deflating membranes (Figure 3), we essentially measure the energy of re-adhesion of a membrane that was previously adhered to the substrate and then separated. The data in Figure 2 are on membranes that were never separated. It appears that after separation, the membranes do not adhere as strongly, leading to smaller values of tension in their final states. Consistent with this, the deflated membranes in Figure 3f exhibit lower Q_{01} values at $\delta_c = 0$ compared with flat membranes of the same radius and thickness that were never pressurized (Figure 2f). Because of higher tension, the resonance frequencies in Figure 2b are typically higher compared to those in Figure 3d, which also results in higher quality factors due to dissipation dilution [39].

We assume that equilibrium exists as the membranes re-adhere to the sidewalls of the microwell in the deflation experiments of Figure 3. Here, we take a continuum view of the polymeric material, even though there may be rearrangements in the molecular-scale disks making up the membrane, leading to entropy changes. This is unlike the situation in 2D crystalline materials, such as graphene, and makes the equilibrium in the system more interesting from a fundamental perspective.

In conclusion, we have explored the device possibilities of a novel 2D material, 2DPA-1, by fabricating and measuring nanomechanical resonators with molecular thicknesses; we have also extracted its material properties and developed complex nanomechanical resonance models with slack and adhesion. Our Γ value for the adhesion of 2DPA-1 on SiO₂ is close to those reported for 2D crystalline materials, such as graphene [40] and MoS₂ [38]. The Young's modulus of 2DPA-1, on the other hand, is one to two orders of magnitude smaller [41, 42]. It remains an open question whether other properties of 2DPA-1 match conventional 1D polymers or crystalline 2D materials.

SUPPORTING INFORMATION

Additional experimental details on resonance and deflection measurements; information on frequency stability; derivation of the spherical-cap model for delaminating membranes; further information on the determination of material properties; and supporting data tables.

ACKNOWLEDGMENTS

We acknowledge support from the US NSF (Grant Nos. CMMI-2001403, CMMI-1934271, and CMMI-2337507). Polymer syntheses and fabrication of pressurized bulge devices were supported by the Center for Enhanced Nanofluidic Transport–Phase 2 (CENT²), an Energy Frontier Research Center funded by the US Department of Energy, Office of Science, Basic Energy Sciences (Grant No. DE-SC0019112).

REFERENCES

- [1] A. N. Cleland and M. L. Roukes, Fabrication of high frequency nanometer scale mechanical resonators from bulk Si crystals, *Appl. Phys. Lett.* **69**, 2653 (1996).
- [2] D. Carr and H. Craighead, Fabrication of nanoelectromechanical systems in single crystal silicon using silicon on insulator substrates and electron beam lithography, *J. Vac. Sci. Technol. B* **15**, 2760 (1997).
- [3] T. Yildirim, L. Zhang, G. P. Neupane, S. Chen, J. Zhang, H. Yan, M. M. Hasan, G. Yoshikawa, and Y. Lu, Towards future physics and applications via two-dimensional material NEMS resonators, *Nanoscale* **12**, 22366 (2020).
- [4] B. Xu, P. Zhang, J. Zhu, Z. Liu, A. Eichler, X.-Q. Zheng, J. Lee, A. Dash, S. More, S. Wu, Y. Wang, H. Jia, A. Naik, A. Bachtold, R. Yang, P. X.-L. Feng, and Z. Wang, Nanomechanical resonators: toward atomic scale, *ACS Nano* **16**, 15545 (2022).
- [5] P. F. Ferrari, S. Kim, and A. M. van der Zande, Nanoelectromechanical systems from two-dimensional materials, *Appl. Phys. Rev.* **10** (2023).
- [6] J. S. Bunch, A. M. Van Der Zande, S. S. Verbridge, I. W. Frank, D. M. Tanenbaum, J. M. Parpia, H. G. Craighead, and P. L. McEuen, Electromechanical resonators from graphene sheets, *Science* **315**, 490 (2007).
- [7] S. J. Cartamil-Bueno, M. Cavalieri, R. Wang, S. Houri, S. Hofmann, and H. S. van der Zant, Mechanical characterization and cleaning of CVD single-layer h-BN resonators, *npj 2D Mater. Appl.* **1**, 16 (2017).
- [8] J. Lee, Z. Wang, K. He, J. Shan, and P. X.-L. Feng, High frequency MoS₂ nanomechanical resonators, *ACS Nano* **7**, 6086 (2013).
- [9] C.-H. Liu, I. S. Kim, and L. J. Lauhon, Optical control of mechanical mode-coupling within a MoS₂ resonator in the strong-coupling regime, *Nano Lett.* **15**, 6727 (2015).
- [10] B. Xu, J. Zhu, F. Xiao, N. Liu, Y. Liang, C. Jiao, J. Li, Q. Deng, S. Wu, T. Wen, S. Pei, H. Wan, X. Xiao, J. Xia, and Z. Wang, Electrically tunable MXene nanomechanical resonators vibrating at very high frequencies, *ACS Nano* **16**, 20229 (2022).
- [11] F. Ye, A. Islam, T. Zhang, and P. X.-L. Feng, Ultra-wide frequency tuning of atomic layer van der Waals heterostructure electromechanical resonators, *Nano Lett.* **21**, 5508 (2021).
- [12] P. Kanjanaboos, X.-M. Lin, J. E. Sader, S. M. Rupich, H. M. Jaeger, and J. R. Guest, Self-assembled nanoparticle drumhead resonators, *Nano Lett.* **13**, 2158 (2013).
- [13] S. Markutsya, C. Jiang, Y. Pikus, and V. V. Tsukruk, Freely suspended layer-by-layer nanomembranes: testing micromechanical properties, *Adv. Funct. Mater.* **15**, 771 (2005).
- [14] X. Wang, T. Yildirim, K. J. Si, A. Sharma, Y. Xue, Q. Qin, Q. Bao, W. Cheng, and Y. Lu, An adaptive soft plasmonic nanosheet resonator, *Laser Photonics Rev.* **13**, 1800302 (2019).
- [15] A. W. McFarland, M. A. Poggi, L. A. Bottomley, and J. S. Colton, Injection moulding of high aspect ratio micron-scale thickness polymeric microcantilevers, *Nanotechnology* **15**, 1628 (2004).
- [16] J. Bunyan and S. Tawfick, Mechanical behavior of PDMS at low pressure, *Mater. Res. Express* **4**, 075306 (2017).
- [17] A. Gaitas and Y. B. Gianchandani, An experimental study of the contact mode AFM scanning capability of polyimide cantilever probes, *Ultramicroscopy* **106**, 874 (2006).
- [18] Y. Yoon, I. Chae, T. Thundat, and J. Lee, Hydrogel microelectromechanical system (MEMS) resonators: beyond cost-effective sensing platform, *Adv. Mater. Technol.* **4**, 1800597 (2019).
- [19] G. Zhang, J. Gaspar, V. Chu, and J. Conde, Electrostatically actuated polymer microresonators, *Appl. Phys. Lett.* **87** (2005).
- [20] U. Adiyan, T. Larsen, J. J. Zárate, L. G. Villanueva, and H. Shea, Shape memory polymer resonators as highly sensitive uncooled infrared detectors, *Nat. Commun.* **10**, 4518 (2019).
- [21] Y. Zeng, P. Gordiichuk, T. Ichihara, G. Zhang, E. Sandoz-Rosado, E. D. Wetzel, J. Tresback, J. Yang, D. Kozawa, Z. Yang, M. Kuehne, M. Quien, Z. Yuan, X. Gong, G. He, D. J. Lundberg, P. Liu, A. T. Liu, J. F. Yang, H. J. Kulik, and M. S. Strano, Irreversible synthesis of an ultrastrong two-dimensional polymeric material, *Nature* **602**, 91 (2022).
- [22] C. L. Ritt, M. Quien, Z. Wei, H. Gress, M. Dronadula, K. Altmisdort, Y.-M. Tu, M. Gadoloff, N. Aluru, K. L. Ekinci, J. S. Bunch, and M. S. Strano, A molecularly impermeable polymer from two-dimensional polyaramids, *Nature* **647**, 383 (2025).
- [23] X. Zhuang, Y. Mai, D. Wu, F. Zhang, and X. Feng, Two-dimensional soft nanomaterials: a fascinating world of

materials, *Adv. Mater.* **27**, 403 (2015).

[24] Y. Ren and Y. Xu, Recent advances in two-dimensional polymers: synthesis, assembly and energy-related applications, *Chem. Soc. Rev.* (2024).

[25] M. Lee, D. Davidovikj, B. Sajadi, M. Šiškins, F. Alijani, H. S. Van Der Zant, and P. G. Steeneken, Sealing graphene nanodrums, *Nano Lett.* **19**, 5313 (2019).

[26] Y. Manzanares-Negro, P. Ares, M. Jaafar, G. López-Polín, C. Gómez-Navarro, and J. Gómez-Herrero, Improved graphene blisters by ultrahigh pressure sealing, *ACS Appl. Mater. Interfaces* **12**, 37750 (2020).

[27] H. R. Ambjørner, A. S. Bjørnlund, T. G. Bonczyk, E. Dollekamp, L. M. Kaas, S. Colding-Fagerholt, K. S. Mølhave, C. D. Damsgaard, S. Helveg, and P. C. K. Vesborg, Thermal dynamics of few-layer-graphene seals, *Nanoscale* **15**, 16896 (2023).

[28] J. S. Bunch, S. S. Verbridge, J. S. Alden, A. M. Van Der Zande, J. M. Parpia, H. G. Craighead, and P. L. McEuen, Impermeable atomic membranes from graphene sheets, *Nano Lett.* **8**, 2458 (2008).

[29] M. Calis, D. Lloyd, N. Boddeti, and J. S. Bunch, Adhesion of 2D MoS₂ to graphite and metal substrates measured by a blister test, *Nano Lett.* **23**, 2607 (2023).

[30] G. Cao and F. An, An innovative approach to characterize the elastic moduli of 2D materials from the central strain of bulged membrane, *Int. J. Mech. Sci.* **274**, 109254 (2024).

[31] H. Gress, J. Barbish, C. Yanik, I. Kaya, R. Erdogan, M. Hanay, M. González, O. Svitelskiy, M. Paul, and K. Ekinci, Multimode Brownian dynamics of a nanomechanical resonator in a viscous fluid, *Phys. Rev. Appl.* **20**, 044061 (2023).

[32] T. Wah, Vibration of circular plates, *J. Acoust. Soc. Am.* **34**, 275 (1962).

[33] W. Weaver Jr, S. P. Timoshenko, and D. H. Young, *Vibration problems in engineering* (John Wiley & Sons, 1991).

[34] A. B. Ari, M. S. Hanay, M. R. Paul, and K. L. Ekinci, Nanomechanical measurement of the Brownian force noise in a viscous liquid, *Nano Lett.* **21**, 375 (2020).

[35] K. Y. Yasumura, T. D. Stowe, E. M. Chow, T. Pfafman, T. W. Kenny, B. C. Stipe, and D. Rugar, Quality factors in micron-and submicron-thick cantilevers, *J. Microelectromech. Syst.* **9**, 117 (2000).

[36] L. Lipiäinen, K. Kokkonen, and M. Kaivola, Homodyne full-field interferometer for measuring dynamic surface phenomena in microstructures, *Opt. Lasers Eng.* **88**, 178 (2017).

[37] S. Timoshenko, *Theory of plates and shells* (McGraw-Hill, 1959).

[38] D. Lloyd, X. Liu, N. Boddeti, L. Cantley, R. Long, M. L. Dunn, and J. S. Bunch, Adhesion, stiffness, and instability in atomically thin MoS₂ bubbles, *Nano Lett.* **17**, 5329 (2017).

[39] N. J. Engelsen, A. Beccari, and T. J. Kippenberg, Ultrahigh-quality-factor micro-and nanomechanical resonators using dissipation dilution, *Nat. Nanotechnol.* **19**, 725 (2024).

[40] S. P. Koenig, N. G. Boddeti, M. L. Dunn, and J. S. Bunch, Ultrastrong adhesion of graphene membranes, *Nat. Nanotechnol.* **6**, 543 (2011).

[41] C. Lee, X. Wei, J. W. Kysar, and J. Hone, Measurement of the elastic properties and intrinsic strength of monolayer graphene, *Science* **321**, 385 (2008).

[42] A. Castellanos-Gomez, M. Poot, G. A. Steele, H. S. van der Zant, N. Agraít, and G. Rubio-Bollinger, Elastic properties of freely suspended MoS₂ nanosheets, *Adv. Mater.* **24**, 772 (2012).

Supporting Information for “Molecularly Thin Polyaramid Nanomechanical Resonators”

Hagen Gress,¹ Cody L. Ritt,² Inal Shomakhov,¹ Kaan Altmisdort,¹ Michelle Quien,³ Zitang Wei,³ John R. Lawall,⁴ Narasimha Boddeti,⁵ Michael S. Strano,^{3,*} J. Scott Bunch,^{1,*} and Kamil L. Ekinci^{1,*}

¹*Department of Mechanical Engineering,
Division of Materials Science and Engineering, and the Photonics Center,
Boston University, Boston, Massachusetts 02215, USA*

²*Department of Chemical and Biological Engineering, University of Colorado Boulder, Boulder, Colorado 80309, USA*

³*Department of Chemical Engineering, Massachusetts Institute of Technology,
Cambridge, Massachusetts 02139, USA*

⁴*National Institute of Standards and Technology, Gaithersburg, Maryland 20899, USA*

⁵*Washington State University, School of Mechanical and Materials Engineering,
Pullman, Washington 99163, USA*

Contents

I. Experimental Details	1
A. Resonance Measurements	1
B. Amplitude Calibration	1
C. Deflection (Bulge Height) Measurements	2
II. Frequency Stability	4
III. Spherical Cap Model	5
A. Tension per Unit Length for a Slacked Membrane	5
B. Application to the Delaminating Membrane	6
C. Pressure inside the Spherical Cap with No Slack	7
D. Strain Energy	7
IV. Determining E, S and ν	9
A. Searching for Both E and S with Fixed $\nu = 0.2$	9
B. Searching for S with Fixed $E = 12.7$ GPa and $\nu = 0.2$	9
C. Effect of Changing ν	9
V. Data Tables	11
References	14

*Email: strano@mit.edu

*Email: bunch@bu.edu

*Email: ekinci@bu.edu

I. EXPERIMENTAL DETAILS

A. Resonance Measurements

We measure the thermal displacement fluctuations of the first four resonant modes with the path-stabilized homodyne Michelson interferometer shown in Figure S1. We use a stabilized HeNe laser with a wavelength of $\lambda \approx 633$ nm and a peak power of 3 mW. The spot size (FWHM) on the sample is about 800 nm, and the incident power is $\sim 600 \mu\text{W}$. We use two photodetectors in our setup. The first detector, PD_1 , measures the vibrations of the membrane. The second photodetector, PD_2 , is part of a feedback loop that stabilizes the interferometer at its point of maximum sensitivity, corresponding to an optical path length difference of $\lambda/4$ between the two arms [S1]. The bandwidth of the feedback loop is less than 400 Hz. After taking a measurement at an antinode of the measured mode, we take a second measurement with the same parameters on the polymer film adjacent to the micowell to determine the background noise level in our measurements, e.g., due to the low-frequency laser noise or cable resonances. For both measurements, we average 10^3 data traces. Based on the assumption that different noise sources are uncorrelated, we subtract our background noise from the noise measured on the membrane.

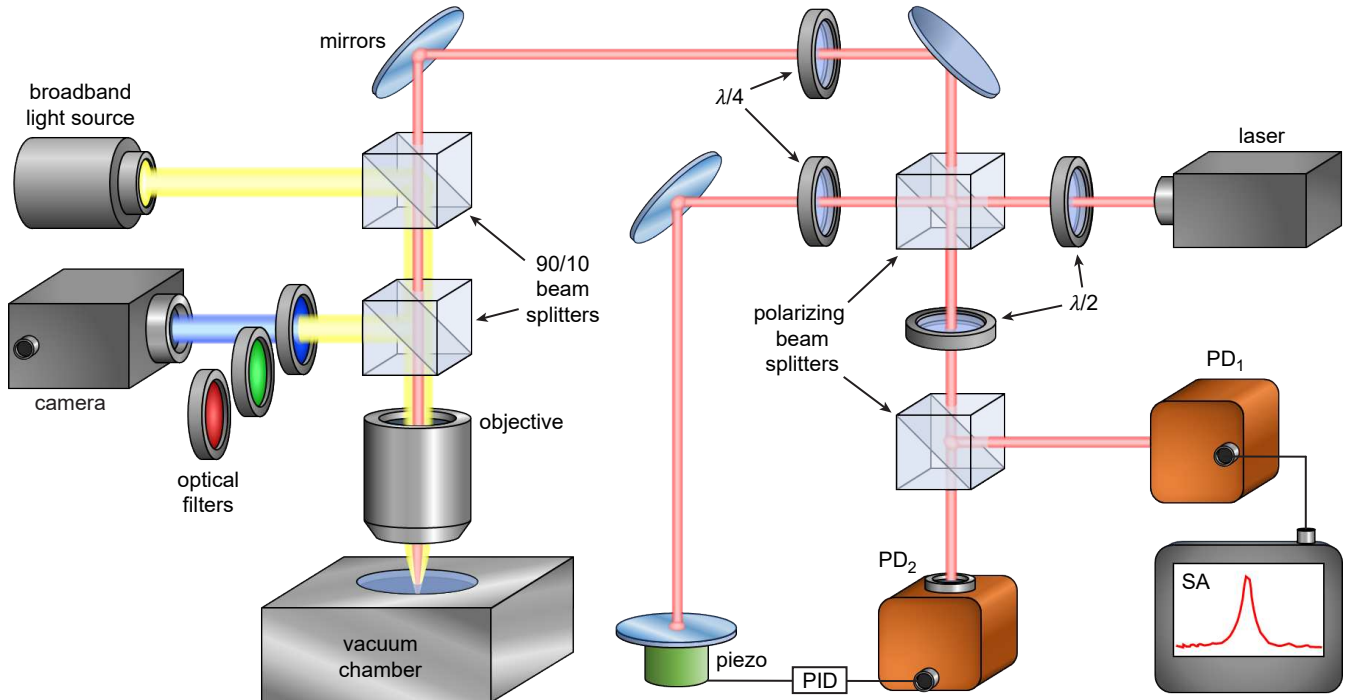


FIG. S1: Schematic of the measurement setup. The displacement fluctuations are measured with a path-stabilized homodyne Michelson interferometer. Simultaneously, the static deflection of pressurized membranes is determined via full-field interferometry using a broadband light source, a camera, and three optical filters. $\lambda/2$: half wave plate; $\lambda/4$: quarter wave plate; PD: photodetector; PID: proportional-integral-derivative controller; SA: spectrum analyzer.

B. Amplitude Calibration

To convert the power spectral density (PSD) of displacement fluctuations from the electrical signal recorded with the spectrum analyzer into units of m^2/Hz as shown in Figure 2a in the main paper, we proceed as follows. For each mode (m, n) , we determine the modal spring constant as

$$k_{mn} = (2\pi f_{mn})^2 m_{mn}, \quad (\text{S1})$$

where f_{mn} is the measured resonance frequency and m_{mn} is the effective modal mass. Assuming that the mode shapes of our resonators can be approximated with those of a circular membrane, we can calculate m_{mn} as [S2]

$$\frac{m_{mn}}{\rho\pi R^2 h} = \begin{cases} [J_1(\alpha'_{0n})]^2 & \text{for } m = 0, \\ \frac{K_m^2}{2} [J_{m+1}(\alpha'_{mn})]^2 & \text{for } m > 0. \end{cases} \quad (\text{S2})$$

Here, ρ is the density, R is the radius, and h is the thickness of the membrane. J_m are Bessel functions of the first kind and K_m are modified Bessel functions of the second kind. The coefficients α'_{mn} are the n^{th} root of J_m .

Once the modal spring constants are known, we calculate the mean-squared fluctuation amplitude $\langle W_{mn}^2 \rangle$ through the equipartition of energy

$$\frac{1}{2}k_{mn}\langle W_{mn}^2 \rangle = \frac{1}{2}k_B T, \quad (\text{S3})$$

where k_B is Boltzmann's constant and T is the temperature. For the plots shown in Figure 2a, all measurements are multiplied with a coefficient such that for each mode the numerical integral over frequency is equal to $\langle W_{mn}^2 \rangle$.

C. Deflection (Bulge Height) Measurements

The semi-transparency of the polymer causes light to be reflected from both the membrane and the bottom of the microwell. We exploit the resulting interference pattern to determine the degree of bulging. Our samples are

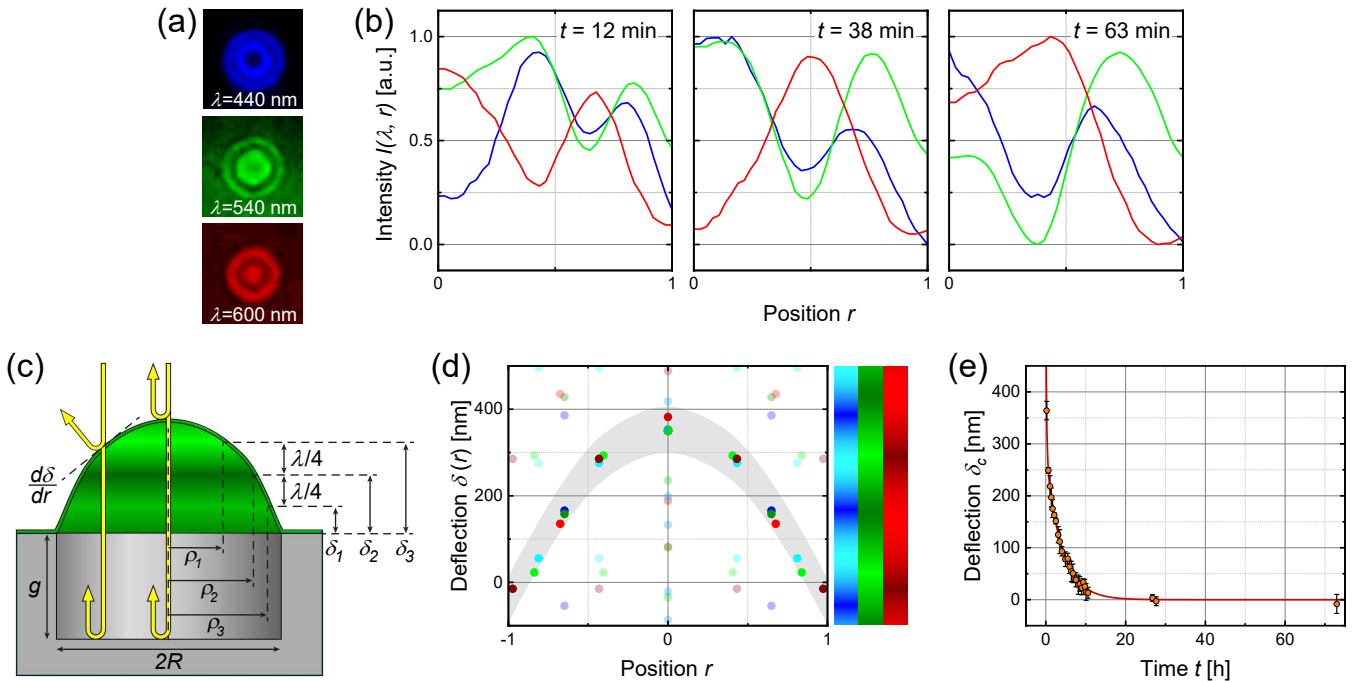


FIG. S2: (a) Interferograms of a bulged-up membrane with thickness $h = 35$ nm after the light passes through three different bandpass filters. (b) Radial intensity profiles for each wavelength at three different points in time. The position is normalized by the radius R of the membrane. Local minima correspond to fringes with destructive interference, and local maxima to fringes with constructive interference. (c) Cross-section of a microwell with a bulged-up membrane. The yellow arrows represent how the direction of the reflected light depends on the local slope $d\delta/dr$ of the membrane. The shading of the membrane corresponds to the interference pattern for $\lambda = 540$ nm. Each fringe with radius ρ_i corresponds to a deflection δ_i . The vertical distance between consecutive fringes is always $\lambda/4$. (d) All solutions to Eqs. (S4) and (S5). Unphysical values are grayed out. For the fringes, bright colors correspond to maxima, dark colors to minima. A representation of the intensity as a function of deflection is shown on the right. The shaded region represents the extrapolated deflection profile $\delta(r)$ of the bulged-up membrane which is used to identify the correct values δ_c at the center. (e) Measured center deflection δ_c of a deflating membrane over time. The data points and error bars are the mean and standard deviation, respectively, of the three values obtained from each wavelength. The red line is an exponential fit.

illuminated with a broadband light source. The reflected light passes through one of three optical bandpass filters with bandwidths $\Delta\lambda \leq 16$ nm and center wavelengths of $\lambda = 440$, 540, and 600 nm, before being recorded on a camera (Figure S1). We calculate the coherence lengths as $L_\lambda = \frac{\lambda^2}{\Delta\lambda}$. For our three filters, we find $L_\lambda = 12.1$, 19.4, and 25.7 μm , respectively. The coherence lengths are therefore larger than the largest difference in optical path length in our experiments, which is $\lesssim 3$ μm for microwells with a depth of $g = 960$ nm and bulges < 500 nm. Examples of interferograms for each wavelength are shown in Figure S2a. We use image processing tools to find the average intensities $I(\lambda, r)$ as a function of the radial position r (Figure S2b). A local maximum corresponds to a constructive (bright) interference fringe and a local minimum to a destructive (dark) one. The deflection $\delta(r)$ can theoretically be determined at any position from $I(\lambda, r)$ if the intensities at destructive and constructive interference, $I_{\min}(\lambda)$ and $I_{\max}(\lambda)$, are known [S1]. However, values for $I_{\min}(\lambda)$ and $I_{\max}(\lambda)$ cannot be easily extracted from local extrema because the amount of light that is reflected back along the optical axis depends on the local slope $d\delta/dr$ (Figure S2c). We therefore combine two different methodologies to determine $\delta(r)$ at all fringes as well as at the center of the membrane, where $d\delta/dr = 0$.

At each interference fringe with radius ρ , the deflection is a solution to

$$\delta(r = \rho) = q \frac{\lambda}{4} - \frac{\lambda}{4\pi} \beta(\lambda) - g, \quad (\text{S4})$$

where the integer q is odd for maxima and even for minima. The quantity $\beta(\lambda)$ accounts for both the phase shift upon reflection at the membrane and the phase shift acquired by two transmissions through the membrane. For a 35-nm-thick membrane with a refractive index of $n \approx 1.57$ [S3], we find $\beta(\lambda) = -0.74$, -0.88 , and -0.95 for the three wavelengths, respectively.

To calculate the deflection δ_c at the center of the membrane, we observe the intensity $I(\lambda, r = 0)$ over time as the membrane gradually deflates (Figure S2b). As long as the total change in optical path length exceeds one wavelength, we can determine $I_{\min}(\lambda)$ and $I_{\max}(\lambda)$ as the lowest and highest measured value, respectively. Assuming that the center point is aligned with the optical axis, the center deflection is then a solution to

$$\delta_c = q \frac{\lambda}{4} \pm \frac{\lambda}{4\pi} \cos^{-1} \left(1 - 2 \frac{I(\lambda, r = 0) - I_{\min}(\lambda)}{I_{\max}(\lambda) - I_{\min}(\lambda)} \right) - \frac{\lambda}{4\pi} \beta(\lambda) - g, \quad (\text{S5})$$

where q is an even integer. We next identify the solutions to Eqs. (S4) and (S5) which match the parabolic deflection profile $\delta(r)$ that we expect based on theory and AFM measurements. To that end, we analyze the interference pattern for each wavelength as follows. Among the solutions to Eq. (S4) for the outermost fringe, we select the value for q that corresponds to the smallest deflection. Working our way towards the center, we increase q by 1 for each subsequent fringe. At the center, we assume that the deflection is within the range of $\delta(r = \rho^*) < \delta_c < \delta(r = \rho^*) + \frac{\lambda}{4}$, where ρ^* is the radius of the smallest observable fringe. We extrapolate $\delta(r)$ (shaded region in Figure S2d) to confirm the validity of our calculations. Our fringe deflections $\delta(r = \rho)$ therefore allow us to identify the correct center deflections δ_c . The reported bulge height is the average of the δ_c values obtained for each wavelength, with a typical standard deviation of ~ 10 nm.

Figure S2e shows the center deflection δ_c of a deflating membrane over time. The data is fit with an exponential function with two time constants. Errors in the optical path length difference due to wall adhesion (main text Figure 1d) or deviations from the nominal microwell depth g can result in an offset of all data points in Figure S2d along the y -axis. We correct for these errors by setting the asymptote of the exponential fit, i.e., the flat membrane, as our reference plane ($\delta_c = 0$ at $t \rightarrow \infty$).

To verify that the membranes are fully deflated at the end of the experiment, we turn to the interferograms corresponding to the last data point (Figure S3a). We assume that $d\delta/dr \approx 0$ across the whole membrane. Therefore, the amount of incident light being reflected back along the optical axis should become independent of position r (Figure S3b). Any deviation from the center deflection can then be estimated as

$$\delta(r) - \delta_c = \pm \frac{\lambda}{4\pi} \left[\cos^{-1} \left(1 - 2 \frac{I(\lambda, r) - I_{\min}(\lambda)}{I_{\max}(\lambda) - I_{\min}(\lambda)} \right) - \cos^{-1} \left(1 - 2 \frac{I(\lambda, r = 0) - I_{\min}(\lambda)}{I_{\max}(\lambda) - I_{\min}(\lambda)} \right) \right]. \quad (\text{S6})$$

Due to the fact that δ_c is monotonically decreasing, the sign in Eq. (S6) is positive when I_{\max} was the last extremum observed during deflation and negative when I_{\min} was the last extremum. Figure S3c shows a deflection measurement of a membrane that is flat. Because the wall of the microwell interferes with the intensity measurements near the edge of the membrane, we focus on the data for $r \lesssim 0.75$ and find that our current setup can determine flatness to within approximately 10 nm.

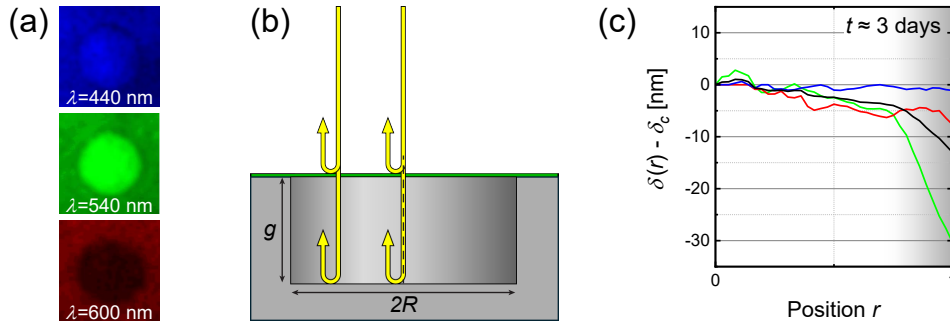


FIG. S3: (a) Interferograms of a presumed flat membrane with thickness $h = 35$ nm after the light passes through three different bandpass filters. (b) Cross-section of a microwell with a flat membrane. The yellow arrows represent how, unlike in a bulged membrane, the amount of light reflected along the optical axis is independent of the radial position r . (c) Deflection profile of a nominally flat membrane relative to its center. The black line represents the average over the three color curves. The gray region indicates where proximity to the wall of the microwell renders the intensity measurement unreliable.

II. FREQUENCY STABILITY

To assess the stability of our resonators, we measured the resonance frequencies f_{01} and quality factors Q_{01} of three 35-nm-thick membranes over three days in air and fourteen days in vacuum. In air, f_{01} and Q_{01} were stable to within 3% and 5%, respectively. After five days in vacuum, the resonance frequencies stabilized to within 10%, whereas the quality factors continuously drifted upward, increasing by 50 – 60%.

III. SPHERICAL CAP MODEL

A. Tension per Unit Length for a Slacked Membrane

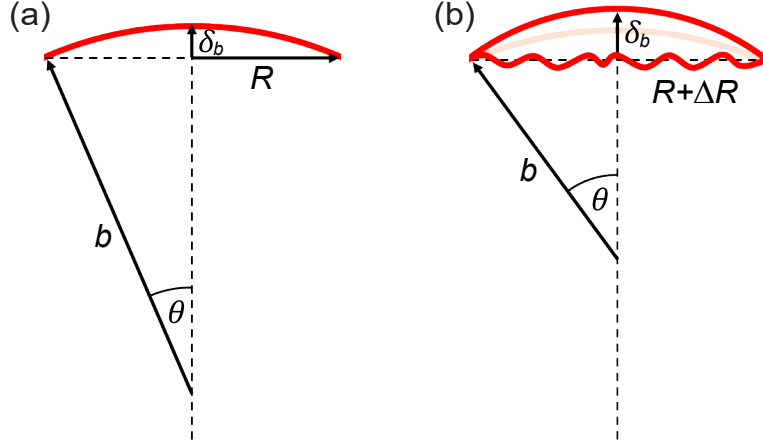


FIG. S4: (a) Spherical cap, where the microwell radius is R , the radius of curvature of the bulge is b , and the height of the bulge at the center is δ_b . We assume that $b \gg R$ and $b \gg \delta_b$. (b) For a slacked membrane, the effective radius exceeds the radius of the microwell by a small length ΔR . This leads to a larger value for δ_b when the membrane is pressurized.

Figure S4a shows the spherical cap geometry for a bulging membrane on a cylindrical microwell of radius R without any slack or pre-tension. We first derive the relationship between the radius of curvature b and the bulge height δ_b at the center through the Pythagorean theorem for the limit $b \gg R$ and $b \gg \delta_b$:

$$b^2 = R^2 + (b - \delta_b)^2 \approx R^2 + b^2 - 2\delta_b b. \quad (\text{S7})$$

Thus,

$$b \approx \frac{R^2}{2\delta_b}. \quad (\text{S8})$$

The biaxial strain ε for this case is

$$\varepsilon \approx \frac{b\theta - R}{R}. \quad (\text{S9})$$

We express the angle θ as a Taylor series expansion as

$$\theta = \arcsin\left(\frac{R}{b}\right) = \frac{R}{b} + \frac{1}{6}\left(\frac{R}{b}\right)^3 + \dots \quad (\text{S10})$$

The strain can then be found as

$$\varepsilon \approx \frac{b\left(\frac{R}{b} + \frac{1}{6}\frac{R^3}{b^3}\right) - R}{R} \approx \frac{R^2}{6b^2}. \quad (\text{S11})$$

Substituting for b from Eq. (S8) above,

$$\varepsilon \approx \frac{R^2}{6\left(\frac{R^2}{2\delta_b}\right)^2} \approx \frac{2}{3}\left(\frac{\delta_b}{R}\right)^2. \quad (\text{S12})$$

For a membrane with slack shown in Figure S4b, the strain is dependent on the effective radius of the membrane,

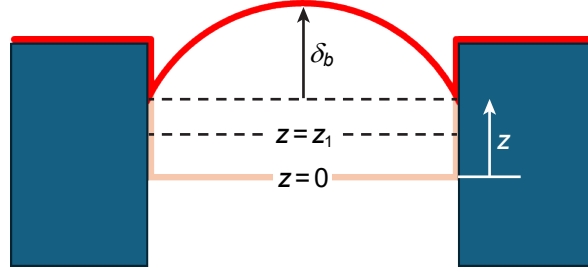


FIG. S5: Schematic of a pressurized membrane in a microwell. At the vertical position $z = 0$, the membrane is completely flat ($\Delta p = 0$) and under tension due to wall adhesion. When the membranes delaminates a distance z_1 due to an applied pressure ($\Delta p > 0$), neither tension due to wall adhesion nor slack exist. For $z > z_1$, slack leads to an increased bulge height δ_b .

$R + \Delta R$, and can be approximated as

$$\begin{aligned} \varepsilon &\approx \frac{b\theta - (R + \Delta R)}{R + \Delta R} \\ &\approx \frac{b \left(\frac{R}{b} + \frac{1}{6} \frac{R^3}{b^3} \right) - (R + \Delta R)}{R + \Delta R} \\ &\approx \frac{R^2}{6b^2 \left(1 + \frac{\Delta R}{R} \right)} - \frac{\Delta R}{R \left(1 + \frac{\Delta R}{R} \right)} \\ &\approx \frac{R^2}{6b^2} - \frac{R\Delta R}{6b^2} - \frac{\Delta R}{R}. \end{aligned} \quad (\text{S13})$$

Substituting for b again,

$$\begin{aligned} \varepsilon &\approx \frac{R^2}{6 \left(\frac{R^2}{2\delta_b} \right)^2} - \frac{R\Delta R}{6 \left(\frac{R^2}{2\delta_b} \right)^2} - \frac{\Delta R}{R} \\ &\approx \frac{2}{3} \left(1 - \frac{\Delta R}{R} \right) \left(\frac{\delta_b}{R} \right)^2 - \frac{\Delta R}{R}. \end{aligned} \quad (\text{S14})$$

The tension per unit length S is related to the strain by

$$S = \frac{Eh}{1-v} \varepsilon. \quad (\text{S15})$$

B. Application to the Delaminating Membrane

In this system, the slack depends on the degree of delamination, as illustrated in Figure S5. Thus, we define a coordinate system z , where $z = 0$ corresponds to the vertical position of the flat membrane ($\Delta p = 0$). The strain in the flat membrane is entirely caused by wall adhesion and can be expressed as $\varepsilon = z_1/R$, where z_1 is the coordinate along the wall such that the tension in the membrane becomes zero if the membrane is flat at that level. When pressure is applied ($\Delta p > 0$), the membrane delaminates a distance z . The bulge height is then $\delta_b = \delta_c - z$, where δ_c is the measured center deflection with respect to the flat state. The delamination reduces the strain component due to adhesion to $\varepsilon = (z_1 - z)/R$ while a second tension component due to bulging, as found in Eq. (S12), is introduced. At the position z_1 , there is no more tension due to wall adhesion. Any further delamination introduces slack and the effective radius of the membrane is increased by $\Delta R = z - z_1$. The strain for $z > z_1$, where a net slack of $\Delta R = z - z_1$ is introduced into the membrane, is determined from Eq. (S14).

Taking these into account and using the ε expressions found above, the tension can be calculated for different regimes of z as follows:

$$S(z) = \begin{cases} \frac{Eh}{1-\nu} \left(\frac{z_1}{R} \right) & \text{for } z = 0. \\ \frac{Eh}{1-\nu} \left[\left(\frac{z_1 - z}{R} \right) + \frac{2}{3} \left(\frac{\delta_c - z}{R} \right)^2 \right] & \text{for } 0 < z \leq z_1. \\ \frac{Eh}{1-\nu} \left[\left(\frac{z_1 - z}{R} \right) + \frac{2}{3} \left(1 - \frac{z - z_1}{R} \right) \left(\frac{\delta_c - z}{R} \right)^2 \right] & \text{for } z > z_1. \end{cases} \quad (\text{S16})$$

We prefer to rewrite the strain and all the length scales in dimensionless units. The dimensionless length scales that we select are $z^* = \frac{z}{R}$, $z_1^* = \frac{z_1}{R}$, and $\delta_c^* = \frac{\delta_c}{R}$.

$$\frac{S(z^*)}{\left(\frac{Eh}{1-\nu}\right)} = \begin{cases} z_1^* & \text{for } z^* = 0. \\ (z_1^* - z^*) + \frac{2}{3}(\delta_c^* - z^*)^2 & \text{for } 0 < z^* \leq z_1^*. \\ z_1^* - z^* + \frac{2}{3}(1 - z^* + z_1^*)(\delta_c^* - z^*)^2 & \text{for } z^* > z_1^*. \end{cases} \quad (\text{S17})$$

In the experiments, the dimensionless length scales typically vary as follows: $0 \lesssim z^* \lesssim 10^{-3}$; $z_1^* \approx 10^{-3}$; and $0 \lesssim \delta_c^* \lesssim 10^{-1}$.

C. Pressure inside the Spherical Cap with No Slack

Assuming biaxial strain, the pressure can be found as follows. The stress σ in a spherical cap with radius b and thickness h can be related to the pressure $\Delta p = p_{in} - p_{out}$ by balancing forces, leading to

$$2\pi Rh\sigma \sin \theta = \pi R^2 \Delta p. \quad (\text{S18})$$

From $\sin \theta = \frac{R}{b}$ and Eq. (S8), we find

$$\Delta p = \frac{2h}{b}\sigma = \frac{4h(\delta_c - z)}{R^2}\sigma. \quad (\text{S19})$$

The stress is related to the strain by

$$\sigma = \frac{E}{1-\nu}\varepsilon = \frac{S}{h} \quad (\text{S20})$$

and therefore has two components: one due to wall adhesion, the other one due to bulging. For $z \leq z_1$, we can combine Eqs. (S16), (S19), and (S20) to determine the pressure as

$$\Delta p = \frac{8Eh}{3(1-\nu)R} \left(\frac{\delta_c - z}{R}\right)^3 + \frac{4Eh}{(1-\nu)R} \left(\frac{z_1 - z}{R}\right) \left(\frac{\delta_c - z}{R}\right). \quad (\text{S21})$$

We add a term to Eq. (S21) to account for the bending rigidity [S4], leading to

$$\Delta p = \frac{8Eh}{3(1-\nu)R} \left(\frac{\delta_c - z}{R}\right)^3 + \frac{4Eh}{(1-\nu)R} \left(\frac{z_1 - z}{R}\right) \left(\frac{\delta_c - z}{R}\right) + \frac{16Eh^3}{3(1-\nu^2)R^3} \left(\frac{\delta_c - z}{R}\right). \quad (\text{S22})$$

Using the dimensionless length scales as above and defining $h^* = \frac{h}{R}$, we write

$$\Delta p = \frac{8E}{3(1-\nu)} h^* (\delta_c^* - z^*)^3 + \frac{4E}{(1-\nu)} h^* (z_1^* - z^*) (\delta_c^* - z^*) + \frac{16E}{3(1-\nu^2)} h^{*3} (\delta_c^* - z^*). \quad (\text{S23})$$

This simplifies to

$$\Delta p = \frac{Eh^*(\delta_c^* - z^*)}{1-\nu} \left[\frac{8}{3}(\delta_c^* - z^*)^2 + 4(z_1^* - z^*) + \frac{16}{3(1+\nu)} h^{*2} \right]. \quad (\text{S24})$$

The typical values for the dimensionless length scales for $z \leq z_1$ are as follows: $h^* \approx 10^{-2}$; $0 \lesssim z^* \lesssim 10^{-3}$; $z_1^* \approx 10^{-3}$; $0 \lesssim \delta_c^* \lesssim 10^{-2}$. In the limit of $z \rightarrow z_1$ ($z^* \rightarrow z_1^*$), we find that $(\delta_c^* - z^*) \sim h^*$, so both the first and third terms inside the brackets need to be taken into account.

D. Strain Energy

In general, the strain energy for the delaminating membrane with *no* slack should be a complicated function of z and δ_c , given that the membrane is stretched both due to bulging and wall adhesion. Here, we will find approximate expressions for the strain energy *only* at the limit of a flat membrane.

For a biaxially strained nearly flat membrane around $z = 0$, the strain energy can be approximated as

$$F_s(z) \approx S(z)\varepsilon(z)\pi R^2. \quad (\text{S25})$$

We do not consider any deformation or stored strain energy in the portion of the membrane that is adhered to the sidewall. We substitute for $S(z)$ and $\varepsilon(z)$ and find

$$F_s(z) \approx \frac{Eh}{1-\nu} \left(\frac{z_1 - z}{R} \right)^2 \pi R^2. \quad (\text{S26})$$

Here, we completely neglected the contribution of the bulging to the energy. We justify this assumption by noting that, as $z \rightarrow 0$, $\delta_c \rightarrow 0$ and the quadratic contribution of the second term in Eq. (S16) to strain becomes even smaller.

IV. DETERMINING E , S AND ν

A. Searching for Both E and S with Fixed $\nu = 0.2$

To find the Young's modulus E and the tension S , we perform a parametric sweep. For each possible combination of E and S , we first calculate the coefficients α and β from

$$\alpha \frac{J_{m+1}(\alpha)}{J_m(\alpha)} + \beta \frac{I_{m+1}(\beta)}{I_m(\beta)} = 0, \quad (\text{S27})$$

where J_m and I_m are the regular and modified Bessel functions of the first kind, respectively, and $\beta = \sqrt{\alpha^2 + SR^2/D}$. We then calculate the theoretical eigenfrequencies

$$f_{mn}^{(t)} = \frac{\alpha_{mn}}{2\pi R} \sqrt{\frac{1}{\rho h}} \sqrt{S + \frac{\alpha_{mn}^2 D}{R^2}}. \quad (\text{S28})$$

for the first four eigenmodes. The density $\rho = 1140 \text{ kg/m}^3$ [S3] as well as the dimensions R and h are known; we take $\nu = 0.2$, assuming a Poisson's ratio similar to that of graphene [S5]. For each measured eigenmode, we calculate the magnitude of the error between the measured and theoretical frequencies as

$$\epsilon_{mn} = \sqrt{\frac{\left(f_{mn} - f_{mn}^{(t)}\right)^2}{f_{mn}^{(t)}}}. \quad (\text{S29})$$

We then find the total (squared) error by summing ϵ_{mn}^2 over all the measured modes. The two-dimensional sweep of E and S reveals the values that minimize the total error. We run the error minimization algorithm for each measured membrane separately, because the value of S is expected to be different from sample to sample.

B. Searching for S with Fixed $E = 12.7 \text{ GPa}$ and $\nu = 0.2$

Figure 2 in the main text shows a large scatter for the Young's modulus E . We therefore investigate the effect of E on the calculated tension S . We take $E = 12.7$ [S6], sweep the value for the tension S , and calculate the corresponding theoretical eigenfrequencies $f_{mn}^{(t)}$ based on Eqs. (S27) and (S28). We calculate the error between the experimental and theoretical eigenfrequencies for each value of S with Eq. (S29). We find S by minimizing the total error. Figure S6a shows the resulting calculated and measured frequencies. Figure S6b shows the ratio between the new tension values S_{new} when E is fixed and the old values S_{old} reported in the main text, when E is also swept. Fixing $E = 12.7 \text{ GPa}$ changes the calculated tension by $< 15\%$. For our thinnest membranes, the bending stiffness becomes negligible. Instead of using Eq. (S28), we therefore compare the experimental frequencies of the 8-nm-thick membranes to those of an ideal membrane

$$f_{mn}^{(t)} = \frac{\alpha'_{mn}}{2\pi R} \sqrt{\frac{S}{\rho h}}, \quad (\text{S30})$$

where α'_{mn} is the n^{th} root of the Bessel function J_m [S7]. The calculated tension differs from the value reported in the main paper by $< 5\%$.

C. Effect of Changing ν

In the main text, we assume that 2DPA-1 has a Poisson ratio similar to graphene and set $\nu = 0.2$. Here, we investigate how much the calculated S depends on the assumed value for ν . We therefore repeat the steps as outlined in Section IV B at a fixed $E = 12.7 \text{ GPa}$ with $\nu = 0.1$ (Figure S6c and S6d) and $\nu = 0.4$ (Figure S6e and S6f). The results for $\nu = 0.1$ are almost identical to those for $\nu = 0.2$. For $\nu = 0.4$, the 65-nm-thick membranes are affected the most, and S changes up to 18% compared to the value reported in the main text.

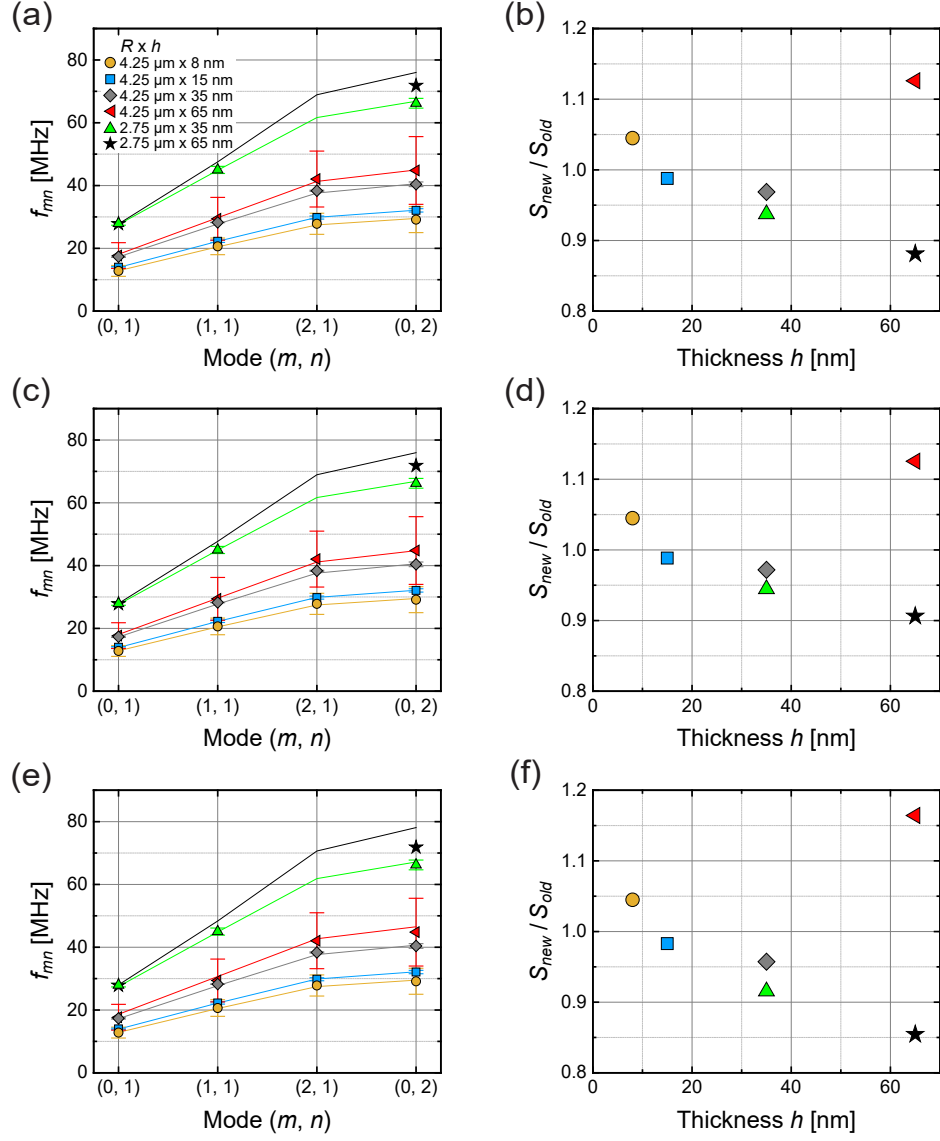


FIG. S6: (a) Resonance frequencies f_{mn} for membranes with indicated R and h , assuming a Young's modulus $E = 12.7$ GPa and a Poisson's ratio $\nu = 0.2$. (b) Ratio of the tension values S_{new} when E is fixed to the tension values S_{old} reported in the main paper when E is also swept. (c) Resonance frequencies f_{mn} and (d) tension ratio S_{new}/S_{old} when the Poisson's ratio is set to $\nu = 0.1$. (e) Resonance frequencies f_{mn} and (f) tension ratio S_{new}/S_{old} when the Poisson's ratio is set to $\nu = 0.4$.

V. DATA TABLES

TABLE S1: Frequencies f_{mn} and quality factors Q_{mn} for the larger resonators with radius $R = 4.25$ μm that were used to calculate the Young's modulus E and the tension S .

		Mode (0, 1)		Mode (1, 1)		Mode (2, 1)		Mode (0, 2)			
h [nm]	Resonator	f_{01} [MHz]	Q_{01} [-]	f_{11} [MHz]	Q_{11} [-]	f_{21} [MHz]	Q_{21} [-]	f_{02} [MHz]	Q_{02} [-]	E [GPa]	S [N/m]
8	1	10.249	914	16.396	917	22.593	849	23.042	640	16.5	0.11
	2	14.344	712	22.839	826	30.700	904	32.632	884	31.0	0.22
	3	13.396	364	21.308	485	28.549	535	30.565	501	27.0	0.19
	4	13.118	887	21.842	1002	28.677	725	29.977	958	27.9	0.19
	5	11.202	1302	17.900	1107	24.319	860	25.236	783	19.0	0.14
	6	14.577	1600	23.221	1555	31.052	1423	33.452	1582	32.1	0.23
	7			23.267	1585	31.324	1591				
	1	13.609	969	21.660	877	28.926	798	31.276	776	8.0	0.37
	2	14.225	658	22.468	870	30.120	737	32.609	665	8.7	0.41
	3	14.081	1004	22.383	1113	29.915	988	32.356	898	8.5	0.40
15	4	13.868	1170	22.039	1230	29.504	1197	31.874	1086	8.3	0.39
	5	14.085	1002	22.382	1103	29.955	1085	32.374	981	8.6	0.40
	6			22.456	1151	30.175	933				
	1	17.601	840	28.199	666	38.203	542	41.324	484	13.2	1.37
	2	17.440	786	-	-	-	-	40.907	488	11.9	1.36
	3	17.386	737	-	-	-	-	40.758	427	11.4	1.35
	4	17.150	976	-	-	-	-	39.877	669	6.9	1.35
	5	17.119	845	-	-	-	-	39.704	608	5.6	1.35
	6	17.005	846	-	-	-	-	39.416	600	5.2	1.34
	7	17.376	1493	-	-	-	-	40.255	965	5.3	1.40
35	8	17.307	1224	-	-	-	-	40.100	860	5.3	1.39
	9	17.229	1043	-	-	-	-	40.002	731	6.2	1.37
	10	17.751	987	-	-	-	-	41.692	552	13.4	1.40
	1	22.426	347	37.074	249	52.095	194	57.173	170	27.1	3.52
	2	15.010	244	37.437	237	52.517	218	37.310	125	11.6	1.60
	3	15.659	177	24.880	165	35.965	138				
	4			-	-	-	-				
	5			-	-	-	-				
	6			-	-	-	-				
	7			-	-	-	-				

TABLE S2: Frequencies f_{mn} and quality factors Q_{mn} for the smaller resonators with radius $R = 2.75$ μm that were used to calculate the Young's modulus E and the tension S . For mode (0, 2), the quality factors could not be determined due to a low signal-to-noise ratio.

		Mode (0, 1)		Mode (1, 1)		Mode (2, 1)		Mode (0, 2)			
h [nm]	Resonator	f_{01} [MHz]	Q_{01} [-]	f_{11} [MHz]	Q_{11} [-]	f_{21} [MHz]	Q_{21} [-]	f_{02} [MHz]	Q_{02} [-]	E [GPa]	S [N/m]
35	1	27.623	579	44.168	387	-	-	65.111	-	6.6	1.40
	2	28.557	460	45.783	312	-	-	67.995	-	9.4	1.46
	3	27.582	389	-	-	-	-	65.508	-	8.0	1.38
65	1	27.825	271	-	-	-	-	71.846	-	8.2	2.20

TABLE S3: Frequencies f_{01} and quality factors Q_{01} for additional resonators for which only the fundamental mode was measured.

h [nm]	R μm	Resonator	Mode (0, 1)		comment
			f_{01} [MHz]	Q_{01} [-]	
35	4.25	1	8.735	396	Figures 3d and 3f at $\delta_c = 0$ nm
		2	9.114	431	Figures 3d and 3f at $\delta_c = 0$ nm
		3	9.207	433	Figures 3d and 3f at $\delta_c = 0$ nm
		4	8.904	454	Figures 3d and 3f at $\delta_c = 0$ nm
		5	8.083	496	Figures 3d and 3f at $\delta_c = 0$ nm
		6	8.768	465	Figures 3d and 3f at $\delta_c = 0$ nm
		7	9.236	443	Figures 3d and 3f at $\delta_c = 0$ nm
		8	7.915	198	Figures 3d and 3f at $\delta_c = 0$ nm
		9	8.198	495	Figures 3d and 3f at $\delta_c = 0$ nm
		10	8.395	537	Figures 3d and 3f at $\delta_c = 0$ nm
		11	8.888	481	Figures 3d and 3f at $\delta_c = 0$ nm
		12	9.070	435	Figures 3d and 3f at $\delta_c = 0$ nm
35	4.25	1	17.781	958	same sample as in Table S1
		2	17.228	445	same sample as in Table S1
		3	17.856	821	same sample as in Table S1
		4	17.335	412	same sample as in Table S1
		5	17.242	317	same sample as in Table S1
		6	18.018	864	same sample as in Table S1
		7	17.278	375	same sample as in Table S1
		8	17.938	895	same sample as in Table S1
		9	17.684	1023	same sample as in Table S1
		10	17.717	1061	same sample as in Table S1
		11	16.953	346	same sample as in Table S1
		12	17.513	1367	same sample as in Table S1
		13	17.548	1366	same sample as in Table S1
		14	17.491	1300	same sample as in Table S1
		15	1703	814	same sample as in Table S1
		16	17.483	1356	same sample as in Table S1
		17	17.437	1201	same sample as in Table S1
		18	17.692	933	same sample as in Table S1
		19	17.419	833	same sample as in Table S1
		20	17.383	722	same sample as in Table S1
		21	17.812	903	same sample as in Table S1
		22	17.711	921	same sample as in Table S1
		23	17.659	914	same sample as in Table S1
		24	17.517	1036	same sample as in Table S1
		25	17.450	1043	same sample as in Table S1
		26	17.444	1107	same sample as in Table S1
65	4.25	1	17.408	238	same sample as in Table S1
		2	14.955	236	same sample as in Table S1
		3	17.017	214	same sample as in Table S1
65	2.75	1	32.855	226	same sample as in Table S2
		2	27.884	250	same sample as in Table S2
		3	27.087	243	same sample as in Table S2
		4	28.080	255	same sample as in Table S2

- [S1] J. W. Wagner, *Phys. Acoust.* **19**, 201 (1990).
- [S2] B. Hauer, C. Doolin, K. Beach, and J. Davis, *Ann. Phys.* **339**, 181 (2013).
- [S3] C. Ritt, M. Quien, Z. Wei, H. Gress, M. Dronadula, K. Altmisdort, Y.-M. Tu, M. Gadaloff, N. Aluru, K. L. Ekinci, J. S. Bunch, and M. S. Strano, *Nature* **647**, 383 (2025).
- [S4] C. Poilâne, P. Delobelle, C. L'Excellent, S. Hayashi, and H. Tobushi, *Thin Solid Films* **379**, 156 (2000).
- [S5] A. Politano and G. Chiarello, *Nano Res.* **8**, 1847 (2015).
- [S6] Y. Zeng, P. Gordiichuk, T. Ichihara, G. Zhang, E. Sandoz-Rosado, E. D. Wetzel, J. Tresback, J. Yang, D. Kozawa, Z. Yang, M. Kuehne, M. Quien, Z. Yuan, X. Gong, G. He, D. J. Lundberg, P. Liu, A. T. Liu, J. F. Yang, H. J. Kulik, and M. S. Strano, *Nature* **602**, 91 (2022).
- [S7] W. Weaver Jr, S. P. Timoshenko, and D. H. Young, *Vibration problems in engineering* (John Wiley & Sons, 1991).